

Latent heat-assisted cooling for high-efficiency solar-driven freshwater production

Received: 26 February 2025

Accepted: 13 November 2025


Published online: 28 November 2025

 Check for updatesYang Guo¹, Nan Hu^{2,3}, Xiaonan Wu¹, Mengxue Zhang¹, Dailin Yang¹, Liwu Fan² & Juan Wang^{1,4}  

Solar-driven interfacial evaporation has shown great potential in freshwater production due to its minimal carbon footprint and adaptability to diverse water sources. However, while significant progress has been made in enhancing vapor generation rates, limited heat dissipation during condensation continues to constrain overall water production efficiency. Here, we introduce a latent heat-assisted evaporative cooling (LHEC) strategy that effectively dissipates condensation heat by harnessing water's latent heat. Using delignified wood as the demonstrating LHEC substrate, we achieved a 2.5-fold increase in heat dissipating heat flux and accelerated vapor diffusion from the evaporation region toward the condensation interface. This approach improves solar water production efficiency to 0.76 (versus 0.49 in conventional systems) and demonstrates robust salt resistance for long-term operation. Notably, the plug-and-play design of the LHEC substrate enables seamless integration into a range of solar evaporation architectures, including single/multi-stage systems, all of which benefit from its enhanced condensation performance. This universality offers a fully passive, single solar-powered solution. This LHEC strategy represents a significant step forward in scalable, efficient and environmentally sustainable freshwater production.

Freshwater is essential for life, agriculture, and industry. However, its scarcity, intensified by climate change, population growth, and industrial expansion, demands urgent solutions through sustainable technologies^{1,2}. Amongst, solar-driven clean water production is particularly attractive due to the abundant and eco-friendly nature of solar energy³. In particular, interfacial solar driven water evaporation strategy which demonstrates excellent solar energy utilization efficiency (>90%) has emerged as a promising sustainable approach, in which solar energy is the only driving force^{4–7}. To date, numerous solar-driven interfacial vapor generation strategies have been developed to enhance vapor generation rates (J_{vapor}), now reaching values of over $1 \text{ kg m}^{-2} \text{ h}^{-1}$ ^{8–10}. However, despite these advancements, the actual clean

water production rate (J_{prod}) remains significantly lower, typically in the range of $0.3\text{--}0.5 \text{ kg m}^{-2} \text{ h}^{-1}$ ^{11–14}. This discrepancy arises primarily from inefficiencies in the vapor-to-liquid condensation process, which is critical for determining the final J_{prod} . For effective condensation, the water vapor must first achieve saturation¹⁵. Unlike the evaporation process typically conducted in open environments, vapor condensation often requires a closed environment to enable vapor saturation (Fig. 1a). However, this closed environment unavoidably increases relative humidity (φ) near the solar evaporator, thereby diminishing the evaporation driving force and, consequently, the evaporation flux ($J_{\text{vapor}} \propto [C_{\text{sat-T(E)}} - \varphi C_{\text{sat-T(S)}}]$). Here, $C_{\text{sat-T(E)}}$ and $C_{\text{sat-T(S)}}$ refer to the vapor saturation concentrations at the temperature of the solar

¹State Key Laboratory of Soil Pollution Control and Safety, Zhejiang University, Hangzhou, China. ²Institute of Thermal Science and Power Systems, School of Energy Engineering, Zhejiang University, Hangzhou, China. ³Department of Mechanical and Aerospace Engineering, Princeton University, Princeton, NJ, USA. ⁴MOE Key Laboratory of Environmental, Remediation and Ecosystem Health, College of Environmental and Resource Sciences, Zhejiang University, Hangzhou, China.  e-mail: wjuan@zju.edu.cn

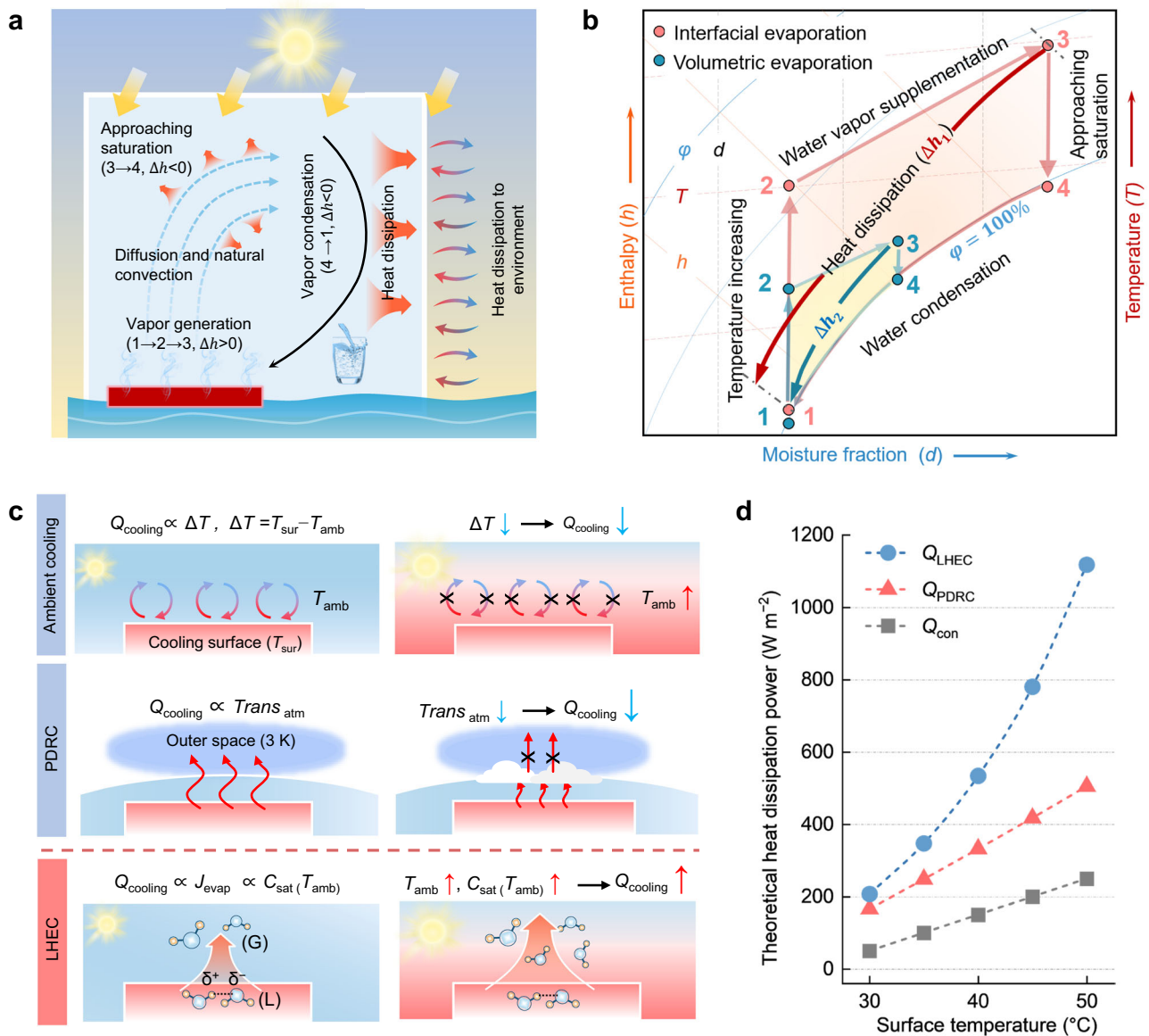


Fig. 1 | Heat dissipation process involved in solar-driven freshwater production within a closed environment. **a** Schematic illustration of the key steps involved in solar-driven freshwater production in a closed environment, highlighting the critical role of heat dissipation. Here h denotes the enthalpy of water vapor, $\Delta h > 0$ denotes the heat absorption by the vapor, $\Delta h < 0$ represents the heat release from vapor. Blue dashed arrows represent the vapor diffusion and convection. **b** Psychrometric chart depicting the closed-loop cycles of volumetric and interfacial evaporation in closed environment, with key parameter changes: 1 → 2 represents air temperature increase at constant moisture fraction, 2 → 3 corresponds to water vapor supplementation via solar evaporation, 3 → 4 indicates vapor saturation through cooling, and 4 → 1 shows moisture fraction reduction due to

water condensation. Δh_1 and Δh_2 denote heat dissipation demands for volumetric and interfacial systems, respectively. **c** Schematic comparison of ambient cooling, passive daytime radiative cooling (PDRC), and latent heat evaporative cooling (LHEC), emphasizing how environmental conditions influence their performance. $Q_{cooling}$ represents the cooling heat flux, T_{sur} is the cooling surface temperature, T_{amb} is the ambient temperature, $Trans_{atm}$ denotes atmospheric transmittance, J_{evap} is the water evaporation flux, and $C_{sat}(T_{amb})$ is the vapor saturation concentration at ambient temperature. **d** Theoretical calculation of cooling power achieved by different strategies as a function of cooling surface temperature, assuming ambient conditions of 25 °C and 50% relative humidity as representative scenarios.

evaporator (T_E) and the surroundings (T_S), respectively^{16,17}. To address this limitation, efficient heat dissipation during condensation can lower $C_{sat-T(S)}$, thereby increasing the evaporation flux and final freshwater production^{16–20}. As illustrated in the psychrometric chart with the closed-air cycle from evaporation to condensation²¹ (Fig. 1b), unlike volumetric evaporation, interfacial solar-vapor generation produces more vapor at a higher temperature. Additionally, the heat generated during the saturation of vapor (step 3 → 4) and vapor-to-liquid phase change (step 4 → 1) is even significantly greater than in conventional volumetric water heating systems, further amplifying the

need for effective heat release. Therefore, a strategy that can efficiently dissipate the heat involved in the above steps is critical to maintaining effective condensation and ultimately boosting the clean water production rate in the interfacial solar clean water production system.

To date, various strategies have been proposed to enhance heat dissipation in solar clean water production systems (Fig. 1c)¹⁴. A widely adopted approach involves using high-thermal-conductivity materials, such as metals (e.g., Cu, Al), in the condensing section to improve convective and conductive heat dissipation (Q_{con})^{20,22–26}. However, this metal-based strategy is expensive, prone to corrosion in water

environments, and becomes less effective at elevated ambient temperature due to the reduced temperature difference between the condenser surface and the surrounding air^{27–29}. Additionally, metals tend to generate parasitic photothermal heat under direct solar irradiation, leading to self-heating and further inhibits heat dissipation, which becomes more severe under hot climates^{30,31}. Another approach utilizes passive daytime radiative cooling (PDRC), which radiates heat into outer space^{32–35}. While PDRC can enhance efficiency to some extent, its overall performance remains low and relies highly on weather conditions^{36–38}. Additionally, the complex material preparation involved increases implementation challenges, hindering large-scale deployment and maintenance³⁹. Therefore, it still remains as a challenge to develop a highly efficient, cost-effective and easily scalable heat dissipation strategy that can perform effectively under high ambient temperature and cloudy weather conditions.

In a typical solar-driven interfacial water evaporation process, heat is absorbed to overcome water's large latent heat of vaporization ($\sim 2450 \text{ J g}^{-1}$), facilitating efficient vaporization⁴⁰. Given the considerable latent heat and continuous water supply, this latent heat can also be harnessed as an effective cooling power source through spontaneous phase transition, to be adopted to dissipate heat and promote vapor condensation (Fig. S14). Unlike ambient cooling and PDRC strategies, the cooling power of latent heat-assisted evaporative cooling (LHEC) increases with the saturated vapor concentration corresponding to the ambient temperature ($C_{\text{sat}}(T_{\text{amb}})$). At a given relative humidity, elevated ambient temperatures lead to higher $C_{\text{sat}}(T_{\text{amb}})$, making LHEC particularly effective in hot climates (Fig. 1c) where conventional cooling methods are less efficient^{41–43}. To evaluate its potential, we conducted theoretical simulations comparing the heat flux of the LHEC process with that of ambient cooling and PDRC (Fig. 1d, see Supplementary Note S1 for detailed calculation)⁴⁴. The results reveal that LHEC achieves a higher heat dissipation flux than both ambient cooling and PDRC, with its cooling advantage becoming more pronounced at elevated surface temperatures. Thus, developing of an all-passive LHEC strategy can overcome the key bottleneck of limited heat dissipation in solar water production systems, offering a promising solution to enhance the solar clean water production efficiency.

In this work, we designed a LHEC strategy by using a delignified wood as the substrate. The wood was chosen for its intrinsic micro-scale tracheids that facilitate water transport and its environmental sustainability. The delignification process significantly enhances water transport capability while reducing solar absorption, minimizing parasitic heat that would otherwise consume additional cooling power. These properties collectively enhance the substrate's heat dissipation performance. Theoretical simulation revealed that the LHEC substrate not only thermodynamically improves heat dissipation, but also kinetically accelerates vapor diffusion from the evaporator interface to the condensation surface, thereby collectively boosting clean water production efficiency. When integrated into a conventional solar interfacial evaporator setup, the LHEC substrate increased the system's heat dissipation capacity by 2.5-fold compared to conventional air cooling. Under solar irradiation of 1.4 kW m^{-2} , the LHEC-assisted system achieved a solar water production efficiency of $\sim 76\%$, compared to $\sim 49\%$ for conventional air-cooling systems. Additionally, this LHEC substrate demonstrates high versatility, seamlessly integrating with various solar interfacial evaporation setups, including single-stage, multi-stage, and geometrically diverse configurations, all of which exhibited improved water production rates. Furthermore, its microporous structure offers resistance to salt accumulation during seawater use, ensuring stable heat dissipation and long-term operational reliability. Compared to existing cooling strategies, the LHEC approach delivers superior efficiency, low cost, sustainability, and environmental adaptability, representing a significant advancement toward practical and scalable solar water production systems.

Results

Design, fabrication and characterization of a wood based latent heat-assisted evaporative cooling substrate

An efficient LHEC process requires substrates that fulfill several key criteria. First, they must exhibit excellent capillary water transport and a large surface area to ensure rapid and stable water evaporation. Second, to minimize parasitic heat accumulation caused by solar energy absorption, the substrates should exhibit low absorption efficiency across the full solar spectrum ($0.2\text{--}2.5 \mu\text{m}$), maintaining a stable and relatively low surface temperature under solar radiation⁴⁵. Third, considering that seawater constitutes around 97% of Earth's water resources, the substrate must have good anti-salt accumulation performance to enable long-term operational stability in marine environments⁴⁶. Considering these requirements, natural wood was chosen as the model material due to its earth-abundant availability and massive intrinsic interconnected channels, which are advantageous for capillary water transport and salt resistance. To further enhance its performance, a delignification treatment was applied to remove lignin, for lowering solar energy absorption capability as well as improving hydrophilicity⁴⁷. The delignified wood exhibits a notably improved whiteness appearance, suggesting its non-absorbing and scattering towards the visible light (Fig. 2a and Fig. S15)^{48,49}. Scanning electron microscopy (SEM) was used to investigate the delignified wood's structure. Cross-sectional SEM images revealed a multi-scale channel network composed of large vessels ($\sim 200 \mu\text{m}$ in diameter) and smaller fiber tracheids ($\sim 20 \mu\text{m}$ in diameter) (Fig. 2b, Figs. S16, S17a). The removal of lignin exposed numerous nanopores ($\sim 100 \text{ nm}$ in diameter) within the wood cell walls, significantly increasing the water transportation channels for water evaporation and enhancing its hydrophilicity (Fig. 2c)⁵⁰. Longitudinal SEM images further revealed the low-tortuous alignment of fiber tracheids, as well as the presence of bordered pits ($\sim 1 \mu\text{m}$ in diameter) distributed across the cell walls (Fig. 2d and Fig. S17b). These pits created interconnections between adjacent vessels and fiber tracheids, facilitating efficient water transport throughout the structure.

The water transport capability of delignified wood was assessed next through dynamic water contact angle tests, showing a contact angle of approximately 57° at 200 ms and complete water droplet absorption within 0.8 sec, confirming its excellent hydrophilicity (Fig. S18). Capillary height measurements further demonstrated the wood's ability to transport water up to 13.2 cm, highlighting its efficient water absorption and transport for LHEC (Fig. 2e). The corresponding thermal-infrared image revealed that after water spread across the delignified wood surface, its temperature dropped to approximately 18°C , with a ΔT of 4°C compared to ambient temperature. The above characteristics indicated that delignified wood can serve as an effective substrate for evaporative cooling.

In addition to supporting evaporative cooling, the hierarchical structure of interconnected channels enhances solar light scattering, reducing parasitic heat detrimental to the LHEC process. Finite-difference-time-domain (FDTD) simulations (Fig. 2f, Note S2) showed that pores with diameter of $10\text{--}30 \mu\text{m}$ can scatter light across the full solar spectrum ($0.2\text{--}2.5 \mu\text{m}$), aligning with the size of the wood's microscale tracheids. This indicates the substrate's ability to effectively scatter sunlight across the entire spectrum. Besides, it shows that nanopores around $1 \mu\text{m}$ contribute to light scattering, particularly in the visible to near-infrared range. The alignment of these pore sizes with the wood's pits and nanopores further enhances overall light scattering efficiency⁴⁷. These multiscale structural features synergistically enhance the substrate's light scattering efficiency, which is critical for reducing parasitic heat^{51,52}. To verify this, solar absorption spectrum of the delignified wood substrate was measured (Fig. 2g), showing a lower solar absorbance (A_{solar}) of approximately 0.11 compared to natural wood (0.46). This result aligns with the above FDTD simulations, demonstrating the substrate's ability to maintain a stable surface

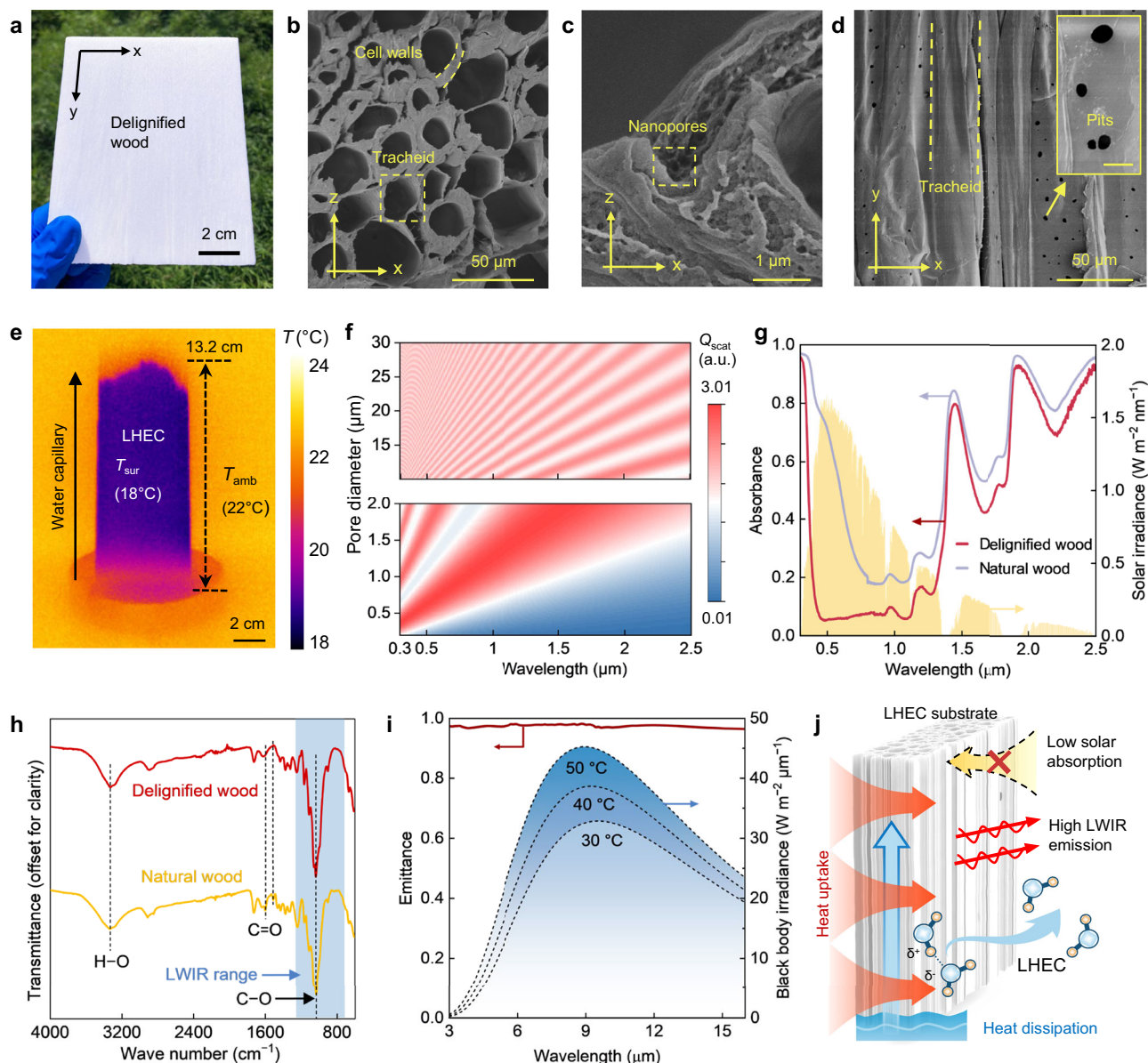


Fig. 2 | Characterization of delignified wood as an LHEC substrate. **a** Optical photograph of delignified wood under natural light. **b–d** Low-resolution scanning electron microscopy images showing the cross-sectional and longitudinal structures of delignified wood, respectively. The insert in **d** provides a magnified view of the pit morphology. Scale bar: 2 μm . **e** Infrared thermal imaging of delignified wood during a water capillary test, with its base submerged in water. **f** Finite-difference time-domain simulation of scattering efficiency (Q_{scat}) for the porous structures in delignified wood across the solar spectrum 0.3–2.5 μm . **g** Spectral absorbance of delignified wood and natural wood at wet state across the full solar spectrum,

overlaid with the AM 1.5 G solar radiation spectrum (yellow). **h** Fourier transform infrared spectroscopy spectra of delignified wood and raw wood. The shaded blue region highlights the long wave infrared range (8–14 μm). **i** Measured long wave infrared emittance spectrum of wet delignified wood, overlaid with blackbody radiance profiles at 30 $^{\circ}\text{C}$, 40 $^{\circ}\text{C}$, and 50 $^{\circ}\text{C}$, representing typical heat dissipation surface temperatures during condensation. **j** Schematic illustrating the function of delignified wood as an LHEC substrate, featuring constant water transport and evaporation, low solar absorption, and effective long wave infrared heat radiation.

temperature and minimize parasitic heat under solar irradiation, thereby supporting efficient LHEC performance.

Besides the above demonstrated potential for efficient LHEC process, the delignified wood can also enhance heat dissipation through radiative cooling, leveraging its intrinsic chemical composition⁴⁷. Fourier transform infrared (FTIR) spectra (Fig. 2h) confirm the removal of lignin, as indicated by the absence of lignin-specific peaks at 1590 and 1501 cm^{-1} . The strong O-H stretching vibration peak at 3350 cm^{-1} reflects abundant hydrophilic sites, consistent with the above water contact angle measurement. The absorption peak at 1103 cm^{-1} corresponds to the numerous C-O

skeletal bonds in the wood structure. This peak falls within the long-wave infrared (LWIR) absorption range (667–1250 cm^{-1}), indicating the wood's ability to radiate heat effectively in this spectrum⁵³. To validate this, we conducted the infrared spectroscopy measurement (Fig. 2i). It shows that the wood substrate achieves a high emittance of ~0.96 across the LWIR range, covering the atmospheric transparent window (8–13 μm), which confirms its strong radiative cooling performance. Furthermore, in typical interfacial vapor condensation scenarios, the heat dissipation surface temperature ranges from 30 to 50 $^{\circ}\text{C}$ ^{54,55}. Theoretical calculation in Fig. 2i indicates that the blackbody radiation peak within this temperature range aligns with the LWIR range,

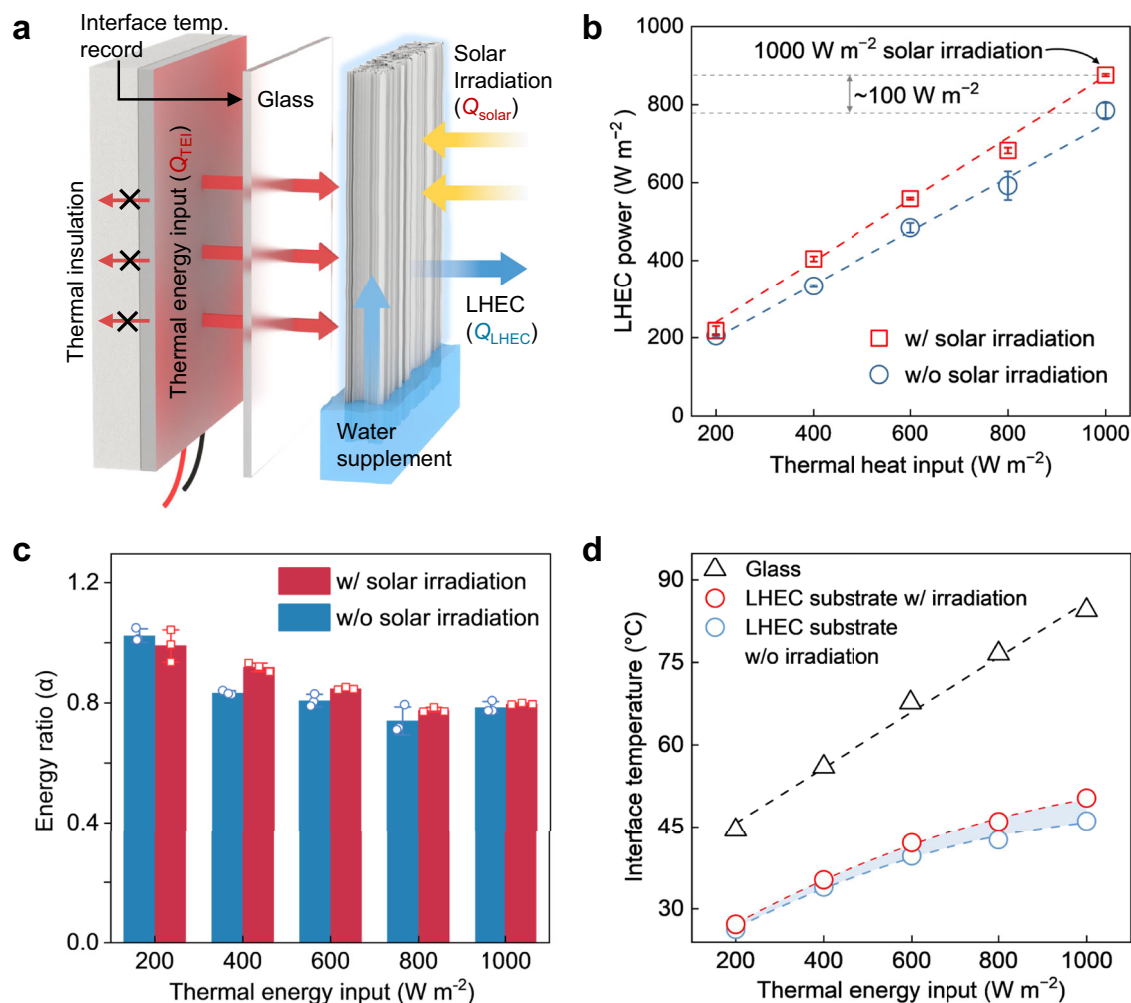


Fig. 3 | Performance evaluation of delignified wood as an LHEC substrate. **a** Schematic of the self-assembled experimental setup for measuring the LHEC performance of delignified wood. Ambient conditions were maintained at 25 °C and 50% relative humidity to simulate typical scenarios. **b** LHEC power profiles of the delignified wood under progressively increased thermal energy inputs, with and without solar irradiation. Experiments were conducted in triplicate, and the error bars represent the arithmetic mean \pm standard deviation. **c** Energy ratio (α) of the LHEC power to the total heat input, calculated under varying thermal energy input,

with and without solar irradiation. The data were derived from Fig. 3c, and the error bars represent the arithmetic mean \pm standard deviation. **d** Monitoring of the condensation interface temperature under different thermal energy input, comparing conventional ambient cooling with the LHEC-assisted cooling strategy with and without solar irradiation. The blue shading represents the temperature difference at the condensation interface under LHEC-assisted cooling, both with and without solar irradiation. Dashed lines in **b**, **d** connect the data points to indicate their trends.

matching the wood's high emittance and further supporting efficient heat dissipation during condensation. By combining the constant evaporative cooling power, low solar absorption and high LWIR emission, the delignified wood demonstrates significant potential as an ideal LHEC substrate for heat dissipation during solar interfacial vapor condensation (Fig. 2j).

Evaluation of the latent heat-assisted evaporative cooling performance

To comprehensively evaluate the delignified wood's performance as an LHEC substrate, its evaporative heat dissipation and anti-parasitic heat capabilities were tested using a self-customized setup (Fig. 3a and Fig. S19). In this setup, an electroheater was used to simulate the heat released during the condensation process by generating thermal energy. A polystyrene (PS) foam was affixed to the backside to reduce heat loss and facilitate faster attainment of thermal equilibrium. A thermal flux meter on the electroheater recorded the corresponding thermal input (Q_{TEI}). On the opposite side, a piece of delignified wood was attached to the glass plate, with a thermocouple placed on the

interface to continuously monitor the "condensation interface" temperature. The bottom side of the wood was immersed in water to ensure a steady water supply for evaporation. A solar simulator was used to irradiate the wood substrate, with its power intensity (Q_{solar}) adjusted to match Q_{TEI} , replicating practical conditions.

As shown in Fig. 3b, the steady LHEC power (Q_{LHEC}) increased proportionally with the thermal energy input (Q_{TEI}), demonstrating the substrates' ability to dissipate heat efficiently through the LHEC process (see Note S3 for detailed LHEC power calculation). To quantify the cooling contribution of the LHEC, we defined the ratio (α) as the proportion of LHEC cooling flux to the total heat input, comprising both the thermal energy input from the electric heater (Q_{TEI}) and the absorbed portion of solar irradiation (Q_{solar}). Therefore, energy ratio α can be calculated using expression $\alpha = \frac{Q_{LHEC}}{Q_{TEI} + A_{solar} \times Q_{solar}}$, where A_{solar} denotes the solar absorbance of LHEC substrate. The measured energy ratio α remained relatively stable, ranging from 0.8 to 1.0 at the thermal input increased from 0.2 to 1 $kW m^{-2}$ (Fig. 3c), indicating that the entire heat dissipation process is predominantly governed by LHEC instead of convective and radiative cooling (Fig. S20). Moreover, the

delignified wood can continuously support this evaporative heat dissipation through rapid water transport, even under high heat loads. It should be mentioned that, under solar irradiation, the LHEC power increased slightly compared to non-irradiated conditions, reflecting the cooling power required to dissipate parasitic heat from solar absorption. Due to the substrate's low solar absorbance, solar irradiation at 1 kW m^{-2} required only $\sim 100 \text{ W m}^{-2}$ of additional cooling (Fig. 3b). This highlights the substrate's ability to scatter solar radiation effectively, as corroborated by its low solar absorbance in Fig. 2f, confirming its resistance to parasitic heat and suitability for efficient LHEC.

Effective heat dissipation can lower the "condensation interface" temperature, which is a critical parameter for thermal management⁵⁶. As shown in Fig. 3d, the interface temperature of LHEC substrate rose more slowly with increasing thermal input and plateaued at higher heat levels. By comparison, a reference glass substrate, which is a common condensation material used in solar interfacial evaporation systems, exhibited consistently higher interface temperature, with the difference becoming more pronounced at higher thermal inputs. These results demonstrate the superior heat dissipation capabilities of delignified wood as LHEC substrate.

Improvement of solar interfacial clean water production by latent heat-assisted evaporative cooling

We integrated the wood-based LHEC substrate into a conventional solar interfacial evaporation setup to evaluate its contribution to clean water production. Considering cost, versatility, earth-abundance and anti-salt fouling, a polypyrrole (PPy)-coated wood interfacial evaporator covered with a conventional glass cover was fabricated as a representative and accessible solar water production setup (see Note S4 for detailed preparation). The PPy-coated evaporator achieved high solar absorption (95%) and a vapor generation rate (J_{evap}) of $\sim 1.11 \text{ kg m}^{-2} \text{ h}^{-1}$ under 1 kW m^{-2} irradiation in an open environment (Figs. S21, S22). The wood-based LHEC substrate was attached to one wall of the cubic glass cover, while a bulk water reservoir below ensured continuous water supply for both solar vapor generation and the LHEC process. The system was tested under simulated solar irradiation to replicate practical real-world conditions (Fig. 4a).

The heat dissipation capability of the LHEC-assisted setup was assessed by comparing heat flux at the LHEC interface to a setup without LHEC. Under varying solar irradiation intensities, both setups showed increasing heat fluxes that stabilized over time (Figs. S23, S24). However, the LHEC-assisted setup consistently demonstrated higher stabilized heat fluxes, with a heat dissipation rate approximately 2.5 times greater than the bare glass surface across different irradiation levels (Fig. 4b). This experimentally highlights the LHEC's significant enhancement of condensation heat dissipation. Additionally, as unveiled by Fig. 4c, temperature monitoring revealed that the LHEC surface was consistently $4\text{--}6 \text{ }^\circ\text{C}$ cooler than the bare glass surface, while the vapor temperature in the LHEC-assisted setup was only slightly lower ($<1 \text{ }^\circ\text{C}$) than in the bare setup. This resulted in a greater temperature difference (ΔT) between the vapor and the condensation wall. Without LHEC, ΔT values range from 6.5 to $11.1 \text{ }^\circ\text{C}$, whereas with LHEC, ΔT increased to $10.0\text{--}16.4 \text{ }^\circ\text{C}$. This improvement in ΔT enhances heat exchange between the vapor and the condensation wall, thereby promoting the condensation process.

The wood-based LHEC substrate not only can enhance heat dissipation but also can accelerate vapor diffusion from the evaporator surface to the condensation section, collectively leading to a higher vapor collection rate. To validate this, we utilized a COMSOL model to simulate the vapor concentration distribution above the evaporator surface, using experimentally measured surface temperature and heat flux values as boundary conditions (see Note S5 and Table S1 for details). As shown in Fig. 4d, the vapor concentration gradient in the LHEC-assisted setup was steeper than in the setup without LHEC. This

steeper gradient confirms faster vapor diffusion in the LHEC-assisted system. The steady vapor diffusion rate (J_{diff}) was calculated using $J_{\text{diff}} = -D \nabla C$, where D is the water vapor diffusion coefficient. Figure 4e shows that J_{diff} in the LHEC-assisted setup was significantly higher, demonstrating enhanced vapor mass transfer from the evaporator surface to the condensation section, which directly benefits the condensation process. Additionally, J_{diff} increased with rising irradiation intensities, consistent with the enlarged temperature difference (ΔT) shown earlier in Fig. 4c.

Clean water generation rates of the two setups were also evaluated. Under 1 kW m^{-2} solar irradiation, the LHEC-assisted setup achieved a freshwater production rate of $0.90 \text{ kg m}^{-2} \text{ h}^{-1}$, representing a 34.3% improvement over the setup without LHEC (Fig. 4f). To evaluate the impact of LHEC coverage, substrates were applied to different sides of the glass cover (Fig. S25). Two-sided coverage yielded the highest water generation rate, while further extension caused evaporator overcooling. Considering this trade-off, along with cost, structural complexity, and potential shading, we adopted the single-sided configuration for subsequent studies. To reveal the contribution of LHEC to energy conversion, we calculated the solar water production efficiency, which is defined as $\eta_{\text{solar-water}} = (J_{\text{prod}} \times H_{\text{cond}}) / I_{\text{solar}}$, where J_{prod} denotes the water generation rate ($\text{kg m}^{-2} \text{ s}^{-1}$), and H_{cond} is the enthalpy of vapor condensation (J kg^{-1}), I_{solar} is the solar irradiation intensity (W m^{-2}). Without LHEC, the solar water production efficiency remained around 45%, which is comparable to the performance of conventional systems^{57,58}. In contrast, the LHEC-assisted setup achieved efficiencies of up to 76% under 1.4 kW m^{-2} , promoting the conversion of solar energy into freshwater (Fig. 4g). Notably, efficiency of the LHEC-assisted setup increased gradually with higher solar intensities, which can be attributed to the increasing heat dissipation benefits of the evaporative cooling mechanism as the heat load increases (Figs. 1d, 3d).

To evaluate the versatility and plug-and-play compatibility of the wood-based LHEC substrate, we integrated it with five representative condensation setups: a single slope device (SSD), an inverted-structure device (ISD), a droplet-wise condensation device (DWD), a film-wise condensation device (FWD), and a three-stage distillation device (TSDD) (see Note S6 for detailed design and preparation). Figure 4h shows that the implementation of the wood based LHEC substrate significantly enhanced water production rates in all setups. Among them, the ISD exhibited the greatest improvement, with a water production rate increase of up to 35.5% under 1 sun irradiation. Meanwhile, the TSDD-LHEC configuration achieved the highest water production rate, reaching $1.99 \text{ kg m}^{-2} \text{ h}^{-1}$. These results demonstrate the LHEC's versatility and effectiveness in enhancing condensation performance across various system designs, highlighting its potential as a robust and adaptable solution for interfacial fresh water production.

Practical performance evaluation of the latent heat-assisted evaporative cooling strategy

An outdoor experiment was conducted to evaluate the practical applicability of the LHEC-assisted solar water production strategy. The experimental setup (Fig. 5a, b) was deployed on the Zijingang Campus of Zhejiang University, Hangzhou, China, from February to May, 2023, under various weather conditions. Thermocouples and a pyranometer were used to continuously monitor and record the ambient temperature and solar intensity profiles. Results for sunny and cloudy conditions both showed that the LHEC-assisted setup consistently outperformed the bare glass setup. On sunny days, the LHEC-assisted system achieved a peak freshwater production rate of $0.85 \text{ kg m}^{-2} \text{ h}^{-1}$ under solar radiation of $\sim 0.9 \text{ kW m}^{-2}$, representing a $\sim 25\%$ increase over the bare setup (Fig. 5c). On cloudy days ($\sim 0.6 \text{ kW m}^{-2}$), the average freshwater production rate improved from 0.40 to $0.54 \text{ kg m}^{-2} \text{ h}^{-1}$, achieving a $\sim 35\%$ improvement (Fig. S26). To further validate the environmental robustness of LHEC strategy, we conducted

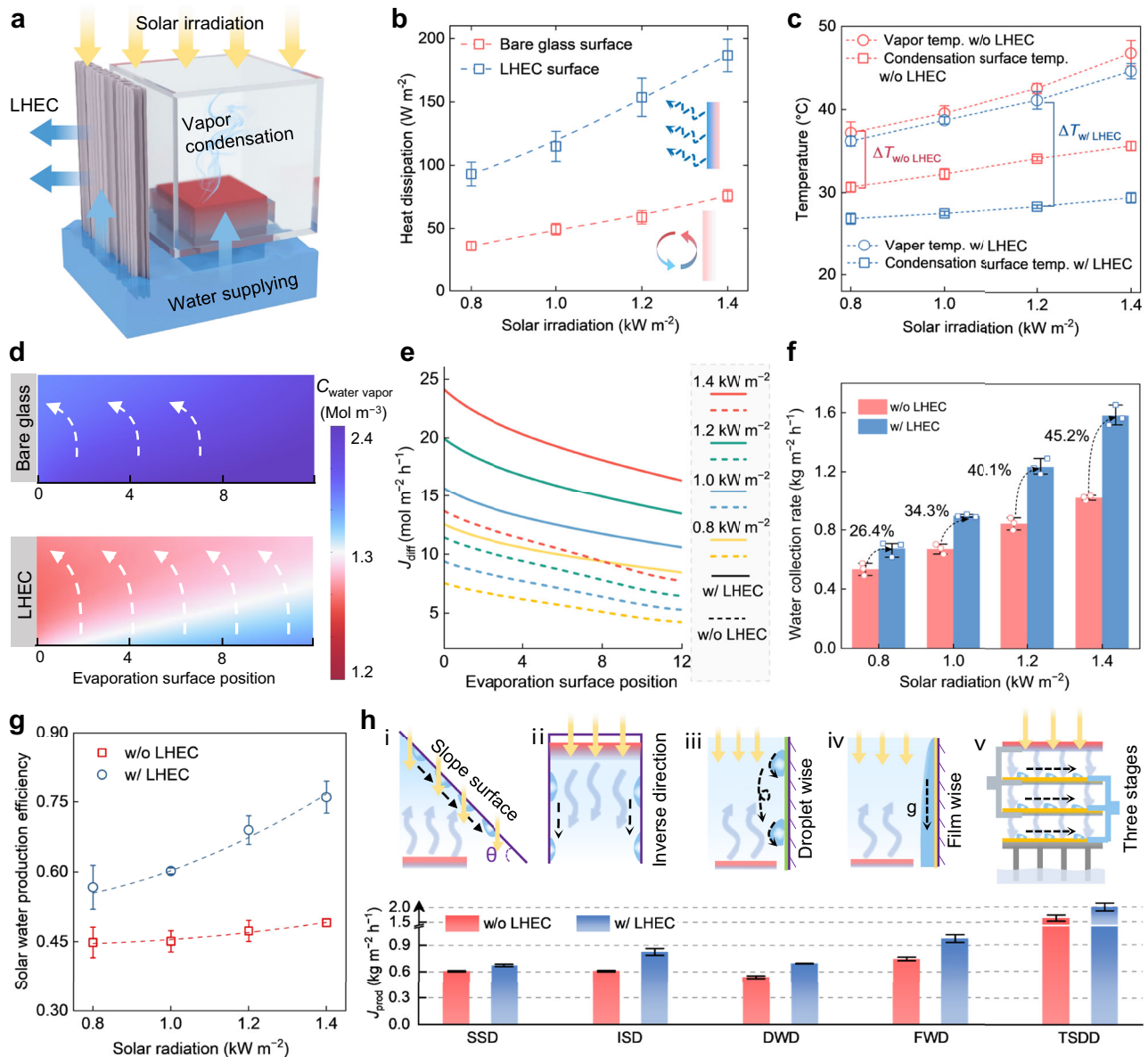


Fig. 4 | Solar water production enhancement with delignified wood LHEC substrate. **a** Schematic diagram of the solar water production setup equipped with a delignified wood LHEC substrate, tested under laboratory conditions of 25 $^{\circ}\text{C}$ and 50% relative humidity. **b** Steady-state heat flux profiles comparing setups with a bare glass surface and the LHEC-equipped surface. **c** Temperature profiles of the condensation surface and generated vapor in setups with and without LHEC assistance. $\Delta T_{w/ \text{ LHEC}}$ and $\Delta T_{w/o \text{ LHEC}}$ denote the temperature differences between the generated vapor and the condensation surface in setups with and without LHEC assistance, respectively. **d** Simulated water vapor concentration distribution near the evaporation region in setups with and without LHEC assistance. $C_{\text{water vapor}}$ represents the water vapor concentration. White arrows represent the direction of

the concentration gradient. **e** Calculated vapor diffusion flux at the evaporation surface based on water vapor concentration distributions, with and without LHEC assistance. **f** Solar freshwater production rates in setups with and without LHEC assistance. **g** Improvement in solar water production efficiency achieved by the LHEC substrate compared to the conventional bare setup. The data were derived from Fig. 4f, and the error bars represent the arithmetic mean \pm standard deviation. **h** Incremental solar water production rates with LHEC assistance across various strategies. Experiments in **b**, **c**, **f**, **h** were conducted in triplicate, and the error bars represent the arithmetic mean \pm standard deviation. Dashed lines in **b**, **c**, **g** connect the data points to indicate their trends.

performance comparisons in a controlled environment chamber with temperatures ranging from 15 to 40 $^{\circ}\text{C}$ and humidity from 25 to 75% RH (Fig. S27). Under these varying conditions, the LHEC strategy consistently provided over a 19% improvement in solar water generation performance. These results demonstrate that the LHEC-assisted strategy can effectively enhance the solar freshwater production under various outdoor conditions.

To test its durability in seawater, simulated seawater (3.5% salinity) was used to evaluate heat dissipation stability (Fig. S28). The wood based LHEC substrate maintained a stable heat dissipation flux of

$\sim 1 \text{ kW m}^{-2}$ over 120 h, under a continued heat load of 1 kW m^{-2} , with no performance decline (Fig. S2d). This stability is attributed to the interconnected multi-scale channel structure of the delignified wood, which facilitates salt re-diffusion and prevents salt accumulation (Fig. S29)⁵⁹. To further validate its practical application, the LHEC-assisted setup was floated on seawater for outdoor testing (Fig. S5e and Fig. S30). It achieved maximum freshwater production rate of $1.08 \text{ kg m}^{-2} \text{ h}^{-1}$ under peak solar irradiance of approximately 1.1 kW m^{-2} (Fig. S5f and Fig. S31). To evaluate scalability, two large-scale solar distillation setups were constructed and tested outdoors using saline

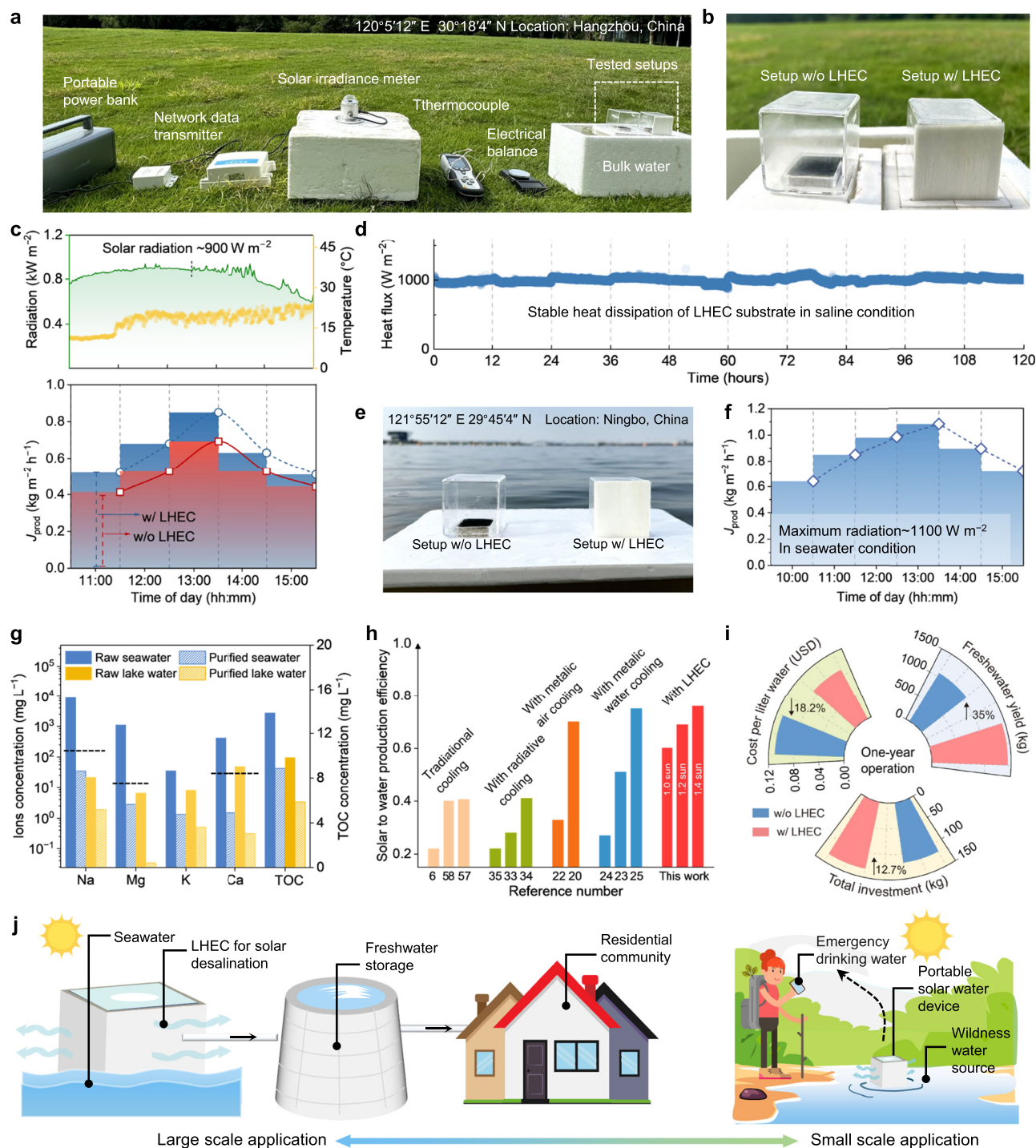


Fig. 5 | Outdoor performance and potential applications of the LHEC-assisted solar freshwater production strategy. **a** Optical photograph of the LHEC-assisted setup and environmental monitoring equipment used for outdoor solar freshwater production tests at Zijingang Campus of Zhejiang University in Hangzhou, China. **b** Photograph of the deployed solar water production setup with and without LHEC assistance. **c** Outdoor environment conditions and corresponding water production rate by setups with and without LHEC under clear, sunny conditions. **d** Intermittent 120-hour monitoring of heat dissipation stability for the LHEC substrate in a brine condition (3.5 wt%) for 10 days. **e** Photograph of the solar water production setups deployed in marine seawater conditions at Meishan Bay,

Ningbo, China. **f** Outdoor solar water production rate for the LHEC-assisted setup operating with seawater in May. **g** Comparison of ion concentrations and total organic carbon (TOC) concentration in raw sea and lake water, and purified water using the LHEC-assisted setup. Black dashed lines mark World Health Organization drinking water quality standards. **h** Comparison of the solar water production efficiency between the LHEC assisted setup and other previously reported works assisted by representative cooling strategies. **i** Economic analysis for setup with and without LHEC over one-year operation. **j** Possible application of the LHEC assisted solar evaporation strategy for floating desalination on seawater and emergency freshwater acquisition in outdoor wilderness scenarios.

water (see Supplementary Note S7 for details). The LHEC-assisted system consistently achieved an average of ~35% increase in water production, confirming its effectiveness at larger scales. Additionally, the water purification performance of the LHEC-assisted setup was evaluated using natural lake water and seawater as raw water sources. The produced freshwater from these sources showed significantly reduced salt ion concentration and total organic carbon (TOC) levels, satisfying World Health Organization (WHO) drinking water standards (Fig. 5g).

We compared the solar water production efficiency of the LHEC-assisted strategy with previously reported approaches (Fig. 5h). The results reveal that despite the simplicity of prototype, the LHEC-assisted system still achieves a notable solar water production efficiency, comparable to state-of-the-art devices. Additionally, we performed an economic analysis of the wood-based LHEC substrate over a one-year operational cycle (Fig. S32 and Table S2 and 3). The results demonstrate that a modest additional investment of 12.7% in materials and maintenance yields a 35% increase in freshwater output, ultimately leading to an 18.2% reduction in the cost per liter of water (Fig. 5i). This low cost suggests that integrating the LHEC strategy into a traditional solar vapor generation system requires minimal investment, yet provides a significant solar water production boost. In summary, the wood-based LHEC strategy demonstrates comparable solar water production efficiency, environmental friendliness, low cost and portability (Tables S4 and 5). These advantages make it an excellent candidate for practical solar water production applications.

Discussion

In this work, we systematically demonstrated the potential of an LHEC strategy to efficiently dissipate heat released during vapor condensation in the interfacial solar evaporation process. Leveraging water's substantial latent heat, this strategy achieves significantly enhanced heat dissipation compared to conventional methods. Using delignified wood as the LHEC substrate, its intrinsic microporous structure and excellent hydrophilicity enable efficient water transport via capillary action, facilitating the evaporative cooling process under solar irradiation. This fully solar-driven dual-evaporative approach achieved a notable increase in solar water production efficiency (0.76 compared to 0.49 in conventional systems), demonstrating its effectiveness. The delignified wood substrate's low cost, environmental sustainability, and portability make it an ideal solution for practical applications, including portable setups for clean water collection from seawater and other surface water sources (Fig. 5j). This all-passive, sustainable strategy potentially offers a versatile and scalable solution to address global clean water challenges.

Methods

Chemicals and materials

Balsa wood was purchased from Sinokiko Balsawood Trading Co., Ltd. (Guangzhou, China). Sodium chlorite (NaClO_2 , 80 wt%) was purchased from Aladdin Ltd. (Shanghai, China). Acetic acid (CH_3COOH , >99.7%) was purchased from RCI Labscan. Sodium acetate (CH_3COONa , >99 wt%) was purchased from J&K Chemical Co., Ltd. (China). Pyridine ($\text{C}_5\text{H}_5\text{N}$, >99.5%) was purchased from MACKLIN Co., Ltd., (China). Ammonium persulfate ($(\text{NH}_4)_2\text{S}_2\text{O}_8$, >98 wt%), Hydrochloric acid (HCl, 36–38%), Octadecyltrichlorosilane ($\text{C}_{18}\text{H}_{37}\text{SiCl}_3$, 95%) and Hexane (C_6H_{14} , >97%) were purchased from Sinopharm Chemical Reagent Co. Ltd. (China). The glass was purchased from Shunlong Quartz Co., Ltd. (Jiangsu, China). All the chemicals and materials were used directly unless otherwise specified.

Fabrication of delignified wood based latent heat-assisted evaporative cooling substrate

To prepare the delignified wood, 2 wt% NaClO_2 solution was first prepared by dissolving NaClO_2 in deionized water. The pH of the

solution was adjusted to 4.8 by adding CH_3COOH and CH_3COONa . Original balsa wood blocks (12 cm × 14 cm) were immersed in this solution and heated at 90 °C for 6 h. This process was repeated three times to ensure effective delignification. After treatment, the wood blocks were sequentially rinsed with ethanol and deionized water to remove residual chemicals. The samples were then frozen at -20 °C for 12 h, followed by lyophilization for 24 h to obtain dry delignified wood.

Characterization

SEM was performed on a field emission scanning electron microscope (Gemini SEM 300, Germany). FTIR spectrometer (AVA TAR370, NICOLET, USA) was employed to conduct the infrared (IR) spectra measurement. The solar absorption spectrum was measured using a UV-vis-NIR spectrophotometer (Cary 5000) with an integrating sphere. The long wavelength IR emittance spectrum was determined using an FTIR spectrometer with an integrating sphere (iS50 FT-IR, NICOLET). The water contact angles were performed using an optical angle meter system (OCA20, Data Physics, Germany). The capillary rise height was determined by the color difference in IR photographs that were taken by an IR camera (FLUK, Ti450, USA).

Quantification of the latent heat-assisted evaporative cooling performance

The latent heat evaporative cooling performance was evaluated using a custom-assembled apparatus. A ceramic heating plate (resistance = 48 Ω) simulated condensation heat, with the heat flux controlled by a DC power supply (Wanptek, GPS305D, China). A heat flux meter (Hukseflux, HFH04-02, Holland) monitored the heat flow density. The LHEC wood substrate was tightly attached to the glass plate (5 cm × 5 cm). Temperature on the inner surface of the glass was measured using thermocouples (CEM, DT8891E, China). The bottom of the LHEC wood substrate was submerged in water contained in a beaker. The mass changes of whole system were measured using an analytical balance (Mettler Toledo, ME 204E, USA) to calculate the evaporation rate. A xenon lamp (CELAAAS50, Aulight) simulated solar irradiation, with intensity adjusted via current and calibrated by an optical power meter (CEL-NP2000-2, Aulight). The experiments were conducted in a laboratory environment with room temperature around 25 °C and relative humidity of ~50%. For each thermal energy input condition, the mass changes of the LHEC substrate were measured in three independent tests, and the error bars represent the arithmetic mean ± standard deviation. The inner surface temperature data under different thermal energy inputs were measured once.

Measurement of solar fresh clean water generation

A typical experiment setup consisted of a delignified wood as the LHEC substrate, a PPy coated wood as the solar evaporator, and a glass cover with a water collection trough. Two thermocouples were placed to measure steam temperature: one on the glass wall at the wood-based LHEC substrate attachment point and the other above the evaporator. A heat flux meter was positioned between the glass wall and the LHEC substrate to measure thermal flux at the condensation surface. The setup was placed over a beaker with deionized water for steam generation and LHEC. Indoor water production experiments were conducted at 25 °C with ~50% relative humidity, while the outdoor experiments were performed on the Zijingang Campus of Zhejiang University, Hangzhou, China, as well as in Meishan Bay, Ningbo, China. A solar radiometer (RS485, China) was employed to record real-time solar radiation, and thermocouples tracked temperature fluctuations. Data were wirelessly transmitted to a personal computer, with the system powered by a portable energy source. Experiments were conducted in triplicate, and the error bars represent the arithmetic mean ± standard deviation.

Data availability

The authors declare that all the data supporting the findings of this study are available within the article (and Supplementary Information Files). All other relevant data supporting the findings of this study are available from the corresponding author upon request. Source data are provided with this paper.

References

- Mekonnen, M. M. & Hoekstra, A. Y. Four billion people facing severe water scarcity. *Sci. Adv.* **2**, e1500323 (2016).
- Vörösmarty, C. J., Green, P., Salisbury, J. & Lammers, R. B. Global water resources: vulnerability from climate change and population growth. *Science* **289**, 284–288 (2000).
- Zhang, Y. & Tan, S. C. Best practices for solar water production technologies. *Nat. Sustain.* **5**, 554–556 (2022).
- Tao, P. et al. Solar-driven interfacial evaporation. *Nat. Energy* **3**, 1031–1041 (2018).
- Ghasemi, H. et al. Solar steam generation by heat localization. *Nat. Commun.* **5**, 4449 (2014).
- Ni, G. et al. A salt-rejecting floating solar still for low-cost desalination. *Energy Environ. Sci.* **11**, 1510–1519 (2018).
- Wang, J. et al. High-performance photothermal conversion of narrow-bandgap Ti₂O₃ nanoparticles. *Adv. Mater.* **29**, 6 (2017).
- Hu, X. et al. Tailoring graphene oxide-based aerogels for efficient solar steam generation under one sun. *Adv. Mater.* **29**, 1604031 (2017).
- Xu, W. et al. Flexible and salt resistant Janus absorbers by electrospinning for stable and efficient solar desalination. *Adv. Energy Mater.* **8**, 1702884 (2018).
- Zhang, L. et al. Highly efficient and salt rejecting solar evaporation via a wick-free confined water layer. *Nat. Commun.* **13**, 849 (2022).
- Zhang, M. et al. KOH activated carbon coated 3D wood solar evaporator with highest water transport height and evaporation rate for clean water production. *Adv. Sci.* **11**, 2402583 (2024).
- Dsilva, W., Rufuss, D., Iniyan, S., Suganthi, L. & Davies, P. A. Solar stills: a comprehensive review of designs, performance and material advances. *Renew. Sust. Energ. Rev.* **63**, 464–496 (2016).
- Chen, K. et al. Simultaneous fresh water collection and Li⁺ selective adsorption enabled by a salt-resistant separated solar evaporator. *Adv. Funct. Mater.* **34**, 2402221 (2024).
- Fu, H. et al. Updates on evaporation and condensation methods for the performance improvement of solar stills. *Energies* **14**, 7050 (2021).
- Moran, M. J., Shapiro, H. N., Boettner, D. D. & Bailey, M. B. *Fundamentals of engineering thermodynamics* (John Wiley & Sons, 2010).
- Zhang, L. et al. Passive, high-efficiency thermally-localized solar desalination. *Energy Environ. Sci.* **14**, 1771–1793 (2021).
- Xu, N. et al. Going beyond efficiency for solar evaporation. *Nat. Water* **1**, 494–501 (2023).
- Li, L. et al. Gradient engineering in interfacial evaporation for water, energy, and mineral harvesting. *Energy Environ. Sci.* <https://doi.org/10.1039/D4EE05239K> (2025).
- Bhardwaj, R., ten Kortenaar, M. V. & Mudde, R. F. Maximized production of water by increasing area of condensation surface for solar distillation. *Appl. Energy* **154**, 480–490 (2015).
- Wang, F. et al. A high-performing single-stage invert-structured solar water purifier through enhanced absorption and condensation. *Joule* **5**, 1602–1612 (2021).
- Bergman, T. L. *Fundamentals of heat and mass transfer* (John Wiley & Sons, 2011).
- Babb, P. I. et al. Salt-rejecting continuous passive solar thermal desalination via convective flow and thin-film condensation. *Cell Rep. Phys. Sci.* **4**, 101682 (2023).
- Han, W., Gao, J., Yu, J., Wang, R. & Xu, Z. Efficient and low-cost solar desalination device with enhanced condensation on nail arrays. *Desalination* **544**, 116132 (2022).
- Du, C. & Huang, C. A floating vapor condensation structure in a heat-localized solar evaporation system for facile solar desalination. *Appl. Therm. Eng.* **201**, 117834 (2022).
- Lan, X. et al. Enhancing the vapor condensation efficiency of a solar water purifier by rapid heat dissipation to bottom bulk water. *J. Mater. Chem. A* **10**, 11784–11792 (2022).
- Zhang, C. et al. Interface chemical coupling enables Janus elastomer-hydrogel composites for a roof-free evaporator with efficient hydrocooling condensation. *J. Mater. Chem. A* **12**, 28273–28282 (2024).
- Liu, R., Liu, L. & Wang, F. The role of hydrostatic pressure on the metal corrosion in simulated deep-sea environments — a review. *J. Mater. Sci. Technol.* **112**, 230–238 (2022).
- Watson, B. J. & Eggert, R. G. Understanding relative metal prices and availability: combining physical and economic perspectives. *J. Ind. Ecol.* **25**, 890–899 (2021).
- Ma, H. et al. Influence of nitrate and chloride ions on the corrosion of iron. *Corrosion* **59**, 1112–1119 (2003).
- Valkonen, E., Karlsson, B. & Ribbing, C. G. Solar optical properties of thin films of Cu, Ag, Au, Cr, Fe, Co, Ni and Al. *Sol. Energy* **32**, 211–222 (1984).
- Paquin, R. A. Properties of metals. *Handb. Opt.* **2**, 35–49 (1995).
- Zhou, M. et al. Vapor condensation with daytime radiative cooling. *Proc. Natl. Acad. Sci. USA* **118**, e2019292118 (2021).
- Chen, M., Li, S., Pang, D. & Yan, H. Selective absorber and emitter boost water evaporation and condensation toward water collection. *Mater. Today Energy* **28**, 101072 (2022).
- Lv, S. et al. Modeling and performance evaluation of radiative cooling-assisted interfacial evaporation for all-day freshwater harvesting. *Desalination* **593**, 118241 (2025).
- Chen, Z., Dong, M. & Wang, C. Passive interfacial photothermal evaporation and sky radiative cooling assisted all-day freshwater harvesting: system design, experiment study, and performance evaluation. *Appl. Energy* **355**, 122254 (2024).
- Zhao, D. et al. Radiative sky cooling: fundamental principles, materials, and applications. *Appl. Phys. Rev.* **6**, 021306 (2019).
- Berdahl, P. Retrospective on the resource for radiative cooling. *J. Photonics Energy* **11**, 042106 (2021).
- Liu, J. et al. Preliminary study of radiative cooling in cooling season of the humid coastal area. *Sol. Energy Mater. Sol. Cells* **208**, 110412 (2020).
- Chen, M., Pang, D., Chen, X., Yan, H. & Yang, Y. Passive daytime radiative cooling: fundamentals, material designs, and applications. *EcoMat* **4**, e12153 (2021).
- Henderson-Sellers, B. A new formula for latent heat of vaporization of water as a function of temperature. *Q. J. R. Meteorol. Soc.* **110**, 1186–1190 (1984).
- Ben Neriah, A., Assouline, S., Shavit, U. & Weisbrod, N. Impact of ambient conditions on evaporation from porous media. *Water Resour. Res.* **50**, 6696–6712 (2014).
- Goodling, J. S., Sill, B. L. & McCabe, W. J. An evaporation equation for an open body of water exposed to the atmosphere. *J. Am. Water Resour. Assoc.* **12**, 843–854 (1976).
- Amer, O., Boukhanouf, R. & Ibrahim, H. A review of evaporative cooling technologies. *Int. J. Environ. Sci. Dev.* **6**, 111 (2015).
- Li, J. et al. A tandem radiative/evaporative cooler for weather-insensitive and high-performance daytime passive cooling. *Sci. Adv.* **8**, eabq0411 (2022).
- Deng, S. et al. Mitigating parasitic absorption in Poly-Si contacts for TOPCon solar cells: a comprehensive review. *Sol. Energy Mater. Sol. Cells* **267**, 112704 (2024).

46. Anis, S. F., Hashaikeh, R. & Hilal, N. Functional materials in desalination: a review. *Desalination* **468**, 114077 (2019).
47. Chen, C. et al. Structure–property–function relationships of natural and engineered wood. *Nat. Rev. Mater.* **5**, 642–666 (2020).
48. Wiersma, D. S. Disordered photonics. *Nat. Photonics* **7**, 188–196 (2013).
49. Li, T. et al. A radiative cooling structural material. *Science* **364**, 760–763 (2019).
50. Dong, Y. et al. Reviewing wood-based solar-driven interfacial evaporators for desalination. *Water Res.* **223**, 119011 (2022).
51. Mandal, J. et al. Hierarchically porous polymer coatings for highly efficient passive daytime radiative cooling. *Science* **362**, 315–319 (2018).
52. Eriksson, T. S., Jiang, S. J. & Granqvist, C. G. Surface coatings for radiative cooling applications: silicon dioxide and silicon nitride made by reactive RF-sputtering. *Sol. Energy Mater.* **12**, 319–325 (1985).
53. Dong, X. et al. Low-value wood for sustainable high-performance structural materials. *Nat. Sustain.* **5**, 628 (2022).
54. Tiwari, G. & Sinha, S. Parametric studies of active regenerative solar still. *Energy Convers. Manag.* **34**, 209–218 (1993).
55. Tiwari, G. & Rao, V. B. Transient performance of a single basin solar still with water flowing over the glass cover. *Desalination* **49**, 231–241 (1984).
56. Nellis, G. & Klein, S. *Heat transfer* (Cambridge University Press, 2008).
57. Yi, L. et al. Scalable and low-cost synthesis of black amorphous Al-Ti-O nanostructure for high-efficient photothermal desalination. *Nano Energy* **41**, 600–608 (2017).
58. Xu, J. et al. Solar-driven interfacial desalination for simultaneous freshwater and salt generation. *Desalination* **484**, 114423 (2020).
59. He, S. et al. Nature-inspired salt resistant bimodal porous solar evaporator for efficient and stable water desalination. *Energy Environ. Sci.* **12**, 1558–1567 (2019).

Acknowledgements

We thank the funding support by the Key Research and Development Project of Science and Technology Department of Zhejiang Province (2025C02213), National Natural Science Foundation of China (22376180, 22176170).

Author contributions

J.W. and Y.G. conceived the project and experiment design. Y.G. conducted the experiments, data analysis, and wrote the original manuscript. Y. G. and N.H. conducted the COMSOL simulation and

psychrometric chart analysis. X.W., M.Z., and D.Y. contributed to the solar water production experiment and manuscript formatting. L.F. contributed to the discussion. J.W. supervised the whole project, commented and revised the manuscript.

Competing interests

The authors declare no competing interests.

Additional information

Supplementary information The online version contains supplementary material available at <https://doi.org/10.1038/s41467-025-66761-1>.

Correspondence and requests for materials should be addressed to Juan Wang.

Peer review information *Nature Communications* thanks Jianfei Zhang, who co-reviewed with Zhiyuan Jiang, and the other, anonymous, reviewer(s) for their contribution to the peer review of this work. A peer review file is available.

Reprints and permissions information is available at <http://www.nature.com/reprints>

Publisher's note Springer Nature remains neutral with regard to jurisdictional claims in published maps and institutional affiliations.

Open Access This article is licensed under a Creative Commons Attribution-NonCommercial-NoDerivatives 4.0 International License, which permits any non-commercial use, sharing, distribution and reproduction in any medium or format, as long as you give appropriate credit to the original author(s) and the source, provide a link to the Creative Commons licence, and indicate if you modified the licensed material. You do not have permission under this licence to share adapted material derived from this article or parts of it. The images or other third party material in this article are included in the article's Creative Commons licence, unless indicated otherwise in a credit line to the material. If material is not included in the article's Creative Commons licence and your intended use is not permitted by statutory regulation or exceeds the permitted use, you will need to obtain permission directly from the copyright holder. To view a copy of this licence, visit <http://creativecommons.org/licenses/by-nc-nd/4.0/>.

© The Author(s) 2025